Joint Design of Transmit Waveform and Receive Filter via ADMM-SFRS

M. M. Omati, S. M. Karbasi and A. Amini

Department of Electrical Engineering
Sharif University of Technology, Tehran, Iran

Abstract

In this paper, we investigate a design method to improve the signal-to-interference-plus-noise ratio (SINR) for an extended target in the presence of signal-dependent interference, while maintaining an energy constraint on the signal. We assume partial knowledge of the target impulse response (TIR), which lies within a predefined uncertainty set, thus addressing a worst-case scenario. Additionally, we impose the constant modulus constraint on the transmit code, which is crucial for radar systems where the transmitter operates near saturation. To design the transmit waveform and receive filter, we use a sequential optimization process, breaking each design problem down, via the alternating direction method of multipliers (ADMM), into a semidefinite programming (SDP) problem and a nonconvex problem with a fixed-rank matrix constraint. For the nonconvex optimization problem, we define the manifold of fixed-rank matrices and then propose a Riemannian steepest descent (RSD) approach within this framework. Our numerical results demonstrate the robustness and effectiveness of the proposed method across various uncertainty sets and target types.

Keywords: Alternating direction method of multipliers (ADMM), extended target model, fixed-rank manifold, max-min optimization, Riemannian steepest descent (RSD).

1. Introduction

The joint optimization of the transmit waveform and the receive filter is a cornerstone challenge in the design of modern radar, sonar, and communication systems [1–25]. This problem has been the subject of extensive research, particularly concerning the development of waveforms for detecting extended targets [1, 5, 6, 11–23]. The primary motivation is the persistent demand for precise target tracking, improved range and Doppler resolution, and robust suppression of noise, signal-dependent interference, and signal-independent interference. Achieving these goals directly leads to increased detection probability [15, 16, 18–20], reduced tracking error [21], and enhanced target identification and classification accuracy [22, 23].

*Corresponding author

Central to this problem is the target's scattering behavior, which is characterized by its target impulse response (TIR). The TIR is determined by the target's physical geometry, its aspect angle (TAA) relative to the radar line-of-sight (LOS), and the operating frequency [5, 6, 26–29].

As a matter of fact, precise knowledge of the exact TIR or its descriptive model can significantly elevate the radar performance [30]. Building on this, various TIR models have been employed for different optimization criteria [31]. The initiative to optimize radar waveforms for extended targets began with [26], exploring waveforms for both optimal detection and information extraction. In the pursuit of an optimal detection waveform, the author of [26] aimed to maximize the output SINR using a deterministic TIR. On the other hand, for information extraction, the TIR was modeled as a random vector, and the design of the transmit waveform focused on maximizing the mutual information (MI) between the TIR and the received signal. Differently, the minimum mean square error (MMSE) metric was employed for TIR parameter estimation or range profiling, as discussed in [28, 29, 32]. Results from [28] demonstrate that minimizing MMSE and maximizing MI yield identical optimal waveforms in an additive white Gaussian channel. These waveform design approaches for extended targets assume precise knowledge of the TIR, which is highly sensitive to target parameters such as TAA. Thus, it is impractical to assume exact knowledge of these factors, and a robust design should account for such uncertainties. One approach to tackle this challenge is to assume that the TIR or power spectral density (PSD) is partially known through cognitive methods [33–35], and then design the transmit waveform and the receive filter. Subsequently, this prompted the development of robust waveforms and filters [1, 5, 6, 36–41]. In [1, 36], waveforms are crafted by maximizing the worst-case SINR under an energy constraint. However, a design focusing solely on the energy constraint is often insufficient for practical implementation, as it disregards crucial waveform properties. For example, such a design provides no control over the signal's temporal structure, potentially leading to high sidelobes in the autocorrelation function, which can obscure smaller targets, or a large peak-to-average power ratio, which is incompatible with transmitter hardware. To address these deficiencies, [42] considers ensuring similarity to a desired reference signal, while [5–7] study the problem of enforcing a constant modulus on the transmitted signal to directly solve the peak-to-average power ratio issue. While both constraints improve practicability, the constant modulus constraint is especially critical from a hardware perspective. It allows the transmitter's power amplifier to operate at maximum efficiency near its saturation point, thereby preventing nonlinear distortion and maximizing the transmitted power [43–45]. The authors of [5, 6, 42] optimized the waveform and filter using a sequential procedure grounded in the semidefinite relaxation (SDR) technique [46]. However, a drawback of these approaches is their sensitivity to the number of

samples. For a small number of samples, these methods exhibit notably reduced SINR performance and reliability compared to direct optimization without relaxation. Furthermore, solving the relaxed version of the optimization problem first and then applying randomization can lead to a suboptimal solution.

2. Contributions

In this study, we propose a robust framework to jointly design the transmit waveform and receive filter for extended targets. The primary objective is to enhance the SINR in the presence of signal-dependent interference and TIR uncertainty. The main contributions of this work are summarized as follows:

- **Robust Joint Design Formulation:** We formulate a worst-case optimization problem that maximizes SINR while strictly adhering to a transmit energy constraint. Crucially, we incorporate a constant modulus constraint for the transmit code—a vital requirement for radar systems operating near saturation. To ensure robustness against estimation errors, we assume partial knowledge of the TIR confined within a predefined uncertainty set.

- **Sequential ADMM-Based Optimization:** We develop a sequential optimization process to design the receive filter $\mathbf{w}$ and the transmit waveform $\mathbf{s}$. To tackle the mathematical complexity, we employ the alternating direction method of multipliers (ADMM) to decompose each design problem into two distinct sub-problems: a convex semidefinite programming (SDP) problem and a non-convex problem subject to a fixed-rank matrix constraint.

- **Riemannian Manifold Algorithm (ADMM-SFRS):** To solve the non-convex sub-problem effectively, we define the geometry of the fixed-rank matrix manifold and propose a Riemannian steepest descent (RSD) approach. This geometric framework allows the algorithm to bypass saddle points and approximate the search space locally as a linear space, yielding superior solutions compared to standard Euclidean approaches.

- **Superior Performance and Convergence:** Numerical simulations demonstrate that the proposed method (ADMM-SFRS) outperforms existing robust techniques and manifold-based nominal designs. Our approach not only achieves higher worst-case SINR across various uncertainty sets and target types but also exhibits significantly faster convergence, requiring fewer iterations and lower overall runtime.

Table 1: List of Acronyms

Acronym	Definition
ADMM	Alternating Direction Method of Multipliers
CIR	Clutter Impulse Response
CM	Constant Modulus
FIR	Finite Impulse Response
ISAC	Integrated Sensing and Communications
LOS	Line-of-Sight
MIMO	Multiple-Input Multiple-Output
RSD	Riemannian Steepest Descent
SDP	Semidefinite Programming
SINR	Signal-to-Interference-plus-Noise Ratio
SISO	Single-Input Single-Output
TAA	Target Aspect Angle
TIR	Target Impulse Response

Notations. We use boldface letters for vectors and matrices: vectors are denoted by lowercase boldface $\mathbf{a}$ and matrices by uppercase boldface $\mathbf{A}$. The transpose operator is indicated by $(.)^T$, and the conjugate transpose by $(.)^\dagger$. The identity matrix is denoted by $\mathbf{I}$, while $\mathbf{0}$ denotes a matrix or vector with all zero entries, with sizes inferred from context. $\mathbf{E}_n$ is considered as a matrix where the $(n,n)^{th}$ element is one and all other entries are zero. The set of N-dimensional complex vectors is represented by $\mathbb{C}^N$, and $\mathbb{H}^N$ denotes the set of $N \times N$ Hermitian matrices. The Euclidean norm of a vector $\mathbf{a}$, and the Frobenius norm of a matrix $\mathbf{A}$ are denoted by $\|\mathbf{a}\|_2$ and $\|\mathbf{A}\|_F$, respectively.The Hadamard product is represented by $\odot$, and the convolution operator by $*$. We denote the objective function and the optimal value of the optimization problem $\mathcal{P}$ as obj($\mathcal{P}$) and $v(\mathcal{P})$, respectively. The expectation operator is represented by $\mathbb{E}[\cdot]$. The symbol $\mapsto$ represents a mapping, where $x \mapsto y$ indicates that x is mapped to y. The symbol $\cong$ denotes isomorphism, indicating equivalence between mathematical structures, as in $\mathcal{A} \cong \mathcal{B}$. Finally, $\mathcal{N}(\mathbf{0}, \mathbf{\Sigma})$ denotes a zero-mean complex Gaussian distribution with covariance matrix $\mathbf{\Sigma}$. For the convenience of the reader, the acronyms employed throughout the manuscript are summarized in Table 1.

3. Target and Signal Model

3.1. Target Model

For radar systems with high range resolution, the range cell size is significantly smaller than the physical dimensions of extended targets whose extent cannot be described by a simple geometric shape such as an ellipse or a rectangle. Therefore, modeling the target as a single-point scatterer is inadequate. Instead, we represent the target by its dominant scattering centers, ensuring that significant returns are confined

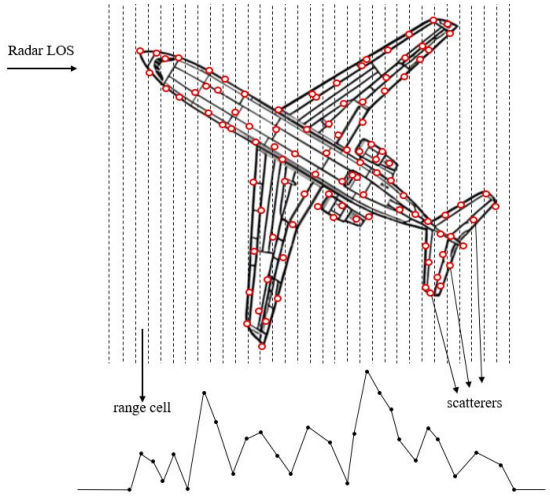

Figure 1: Return wave from scattering centers located in the range of radar visibility.

to specific range cells along the radar's LOS. To model this accurately, the target is treated as a linear system with a finite impulse response (FIR), where the parameters are based on the target's shape and LOS [47–49]. Slight changes in the target's orientation can complicate the identification and detection of these scatterers. Fig. 1 demonstrates how TIR is formed by projecting the scattering centers onto the LOS.

3.2. Signal Model

We consider a monostatic single-input single-output (SISO) radar setup where the transmitter signal is represented by an N-dimensional fast time code:

$$\mathbf{s} = [s(0), ..., s(N-1)]^T \in \mathbb{C}^N. \tag{1}$$

In scenarios where the target is surrounded by clutter, we can express the discrete-time baseband equivalent of the return signal from the extended target as follows:

$$\begin{aligned} r(n) &= \sum_{k=0}^{N-1} [h_\theta(n-k) + c(n-k)]s(k) + v\,(n) \\ &= [h_\theta(n) + c(n)] * s(n) + v\,(n). \end{aligned} \tag{2}$$

Note that (2) represents the baseband equivalent signal after range alignment to the target range bin, assuming negligible Doppler-induced phase variations within the pulse duration, consistent with standard waveform design formulations [6, 50]. Here, the variable n represents the discrete time index, while $h_\theta(n)$

denotes the TIR associated with the TAA θ. Here, $h_\theta(n)$ is assumed to have a support interval of length Q, implying that $h_\theta(n) = 0$ unless n belongs to the set $\{0, \ldots, Q-1\}$. The term $c(n)$ represents the clutter impulse response (CIR), while $v(n)$ signifies receiver noise.

Let us denote the TIR vector by $\mathbf{h}_\theta = [h_\theta(0), \ldots, h_\theta(Q-1)]^T \in \mathbb{C}^Q$. Additionally, we collect all observations $r(n)$ of the desired target and organize them into a vector $\mathbf{r} = [r(0), \ldots, r(M-1)]^T \in \mathbb{C}^M$, where $M = Q + N - 1$ represents the total number of discrete time observations. This observation vector can be represented as:

$$\mathbf{r} = \mathbf{H}_\theta \mathbf{s} + \mathbf{C}\mathbf{s} + \boldsymbol{v}, \tag{3}$$

where $\boldsymbol{v} = [v(0), \ldots, v(M-1)]^T$ is the additive noise component, $\mathbf{C} = \sum_{n=-N+1}^{M-1} c(n)\mathbf{J}_n$ and $\mathbf{H}_\theta = \sum_{n=0}^{q-1} h_\theta(n)\mathbf{J}_n$ are, respectively, the CIR and the TIR matrices, with $\mathbf{J}_n$ being the $M \times N$-dimensional shift matrix:

$$\mathbf{J}_n(\alpha_1, \alpha_2) = \begin{cases} 1, & \text{if} \quad \alpha_1 - \alpha_2 = n \\ 0, & \text{if} \quad \alpha_1 - \alpha_2 \neq n \end{cases}, \tag{4}$$

$$\alpha_1 = \{1, 2, .., M\}, \alpha_2 = \{1, 2, .., N\}. \tag{5}$$

We consider that the noise vector $\boldsymbol{v}$ is circularly symmetric with the following statistical characteristics:

$$\mathbb{E}[\boldsymbol{v}] = \mathbf{0}, \tag{6}$$

$$\boldsymbol{\Sigma}_{\boldsymbol{v}} = \mathbb{E}[\boldsymbol{v}\boldsymbol{v}^\dagger] = \sigma_{\boldsymbol{v}}^2 \mathbf{I}, \tag{7}$$

where $\sigma_{\boldsymbol{v}}^2$ represents the variance of each filtered noise sample. Additionally, we assume that clutter has a zero mean, i.e., $\mathbb{E}[c(n)] = 0$, and is independent of the noise random process.

Due to the high sensitivity of TIR to TAA, providing an exact specification of TIR may not reflect reality accurately. Therefore, the true TIR is considered to belong to a finite uncertainty set $\mathcal{I}$, obtained by sampling the TIR across possible TAAs. We proceed by defining the uncertainty set $\mathcal{I}_{\phi_1}^{\phi_2}$ of length K as: $\mathcal{I}_{\phi_1}^{\phi_2} = \{k\Delta\theta \mid k \in \mathbb{Z}, k\Delta\theta \in [\phi_1, \phi_2]\}$, where $\Delta\theta$ denotes the TAA sampling step. Our goal is to optimize the waveform-filter pair to maximize the worst-case SINR over the defined uncertainty set of TIRs. We will elaborate on the formulation of this worst-case optimization problem in the subsequent section.

4. Problem Formulation

In this section, our focus lies on formulating the problem for designing the waveform-filter pair. If we assume that the observation vector $\mathbf{r}$ is filtered through $\mathbf{w} = [w(0), ..., w(M-1)]^T \in \mathbb{C}^M$, then the SINR at the filter output can be expressed as:

$$\mathrm{SINR}_\theta(\mathbf{s}, \mathbf{w}) = \frac{\left|\mathbf{w}^\dagger \mathbf{H}_\theta \mathbf{s}\right|^2}{\mathbb{E}\left[\left|\mathbf{w}^\dagger \mathbf{C}\mathbf{s}\right|^2\right] + \mathbb{E}\left[\left|\mathbf{w}^\dagger \boldsymbol{\upsilon}\right|^2\right]}. \tag{8}$$

To ensure the transmitter operates efficiently near its saturation region, we enforce a constant modulus constraint on the transmit signal $\mathbf{s}$. Specifically, we require $|s(n)| = \frac{1}{\sqrt{N}}$ for each element n. As a result, the worst-case optimization problem can be formulated as:

$$\mathcal{P}: \begin{cases} \max\limits_{\mathbf{s},\mathbf{w}} \min\limits_{\theta \in \mathcal{I}_{\phi_1}^{\phi_2}} & \mathrm{SINR}_\theta(\mathbf{s}, \mathbf{w}) \\ \text{s.t.} & \|\mathbf{s}\|_2^2 = 1 \\ & |s(n)|^2 = \dfrac{1}{N}, \quad n = 0, ..., N-1. \end{cases} \tag{9}$$

Let us define the rank-one code and filter matrices as $\mathbf{S} = \mathbf{s}\mathbf{s}^\dagger$ and $\mathbf{W} = \mathbf{w}\mathbf{w}^\dagger$, respectively. With these definitions, we obtain two equivalent expressions for (8):

$$\mathrm{SINR}_\theta(\mathbf{s}, \mathbf{w}) = \frac{\mathbf{w}^\dagger \boldsymbol{\Gamma}(\mathbf{H}_\theta, \mathbf{S})\mathbf{w}}{\mathbf{w}^\dagger \boldsymbol{\Sigma}_{\mathbf{C}\boldsymbol{\upsilon}}(\mathbf{S})\mathbf{w}} = \frac{\mathbf{s}^\dagger \bar{\boldsymbol{\Gamma}}(\mathbf{H}_\theta, \mathbf{W})\mathbf{s}}{\mathbf{s}^\dagger \bar{\boldsymbol{\Sigma}}_{\mathbf{C}\boldsymbol{\upsilon}}(\mathbf{W})\mathbf{s}}, \tag{10}$$

where

$$\boldsymbol{\Gamma}(\mathbf{H}_\theta, \mathbf{S}) = \mathbf{H}_\theta \mathbf{S} \mathbf{H}_\theta^\dagger, \tag{11}$$

$$\boldsymbol{\Sigma}_{\mathbf{C}\boldsymbol{\upsilon}}(\mathbf{S}) = \mathbb{E}\left[\mathbf{C}\mathbf{S}\mathbf{C}^\dagger\right] + \sigma_{\boldsymbol{\upsilon}}^2 \mathbf{I}, \tag{12}$$

$$\bar{\boldsymbol{\Gamma}}(\mathbf{H}_\theta, \mathbf{W}) = \mathbf{H}_\theta^\dagger \mathbf{W} \mathbf{H}_\theta, \tag{13}$$

$$\bar{\boldsymbol{\Sigma}}_{\mathbf{C}\boldsymbol{\upsilon}}(\mathbf{W}) = \mathbb{E}[\mathbf{C}^\dagger \mathbf{W} \mathbf{C}] + \sigma_{\boldsymbol{\upsilon}}^2 \mathrm{tr}(\mathbf{W})\mathbf{I}. \tag{14}$$

A detailed explanation of the SINR formulation in (10) is derived in the Appendix 7.1.

In the following section, we discuss our proposed methodologies for finding the optimal solutions for the receive filter $\mathbf{w}$ and the transmit waveform $\mathbf{s}$ for the worst-case problem $\mathcal{P}$.

5. Design of the waveform-filter pair

In this section, our focus is on discussing the joint optimization of the receive filter $\mathbf{w}$ and the transmit waveform $\mathbf{s}$. This is achieved through alternating optimization of the receive filter $\mathbf{w}$ and transmit waveform $\mathbf{s}$. Initially, we concentrate on optimizing the receive filter $\mathbf{w}$ while keeping $\mathbf{s}$ fixed. Then, we shift our focus to optimizing the transmit signal $\mathbf{s}$, assuming a fixed receive filter $\mathbf{w}$.

Upon examining optimization problem $\mathcal{P}$, we notice that scaling $\mathbf{w}$ by a constant does not affect the objective function, as it equally affects both the numerator and denominator. Therefore, we can introduce an additional constraint $\|\mathbf{w}\|_2^2 = 1$ to our optimization problem. Consequently, when solving the optimization problem alternately, we have:

$$\mathcal{P}_{\mathbf{w}}^{(m)}: \quad \begin{cases} \max\limits_{\mathbf{w}} \min\limits_{\theta} & \dfrac{\mathbf{w}^\dagger \mathbf{\Gamma}(\mathbf{H}_\theta, \mathbf{S}^{(m-1)})\mathbf{w}}{\mathbf{w}^\dagger \mathbf{\Sigma}_{\mathbf{C}\boldsymbol{\upsilon}}(\mathbf{S}^{(m-1)})\mathbf{w}} \\ \text{s.t.} & \|\mathbf{w}\|_2^2 = 1, \end{cases}$$

$$\mathcal{P}_{\mathbf{s}}^{(m)}: \quad \begin{cases} \max\limits_{\mathbf{s}} \min\limits_{\theta} & \dfrac{\mathbf{s}^\dagger \bar{\mathbf{\Gamma}}(\mathbf{H}_\theta, \mathbf{W}^{(m)})\mathbf{s}}{\mathbf{s}^\dagger \bar{\mathbf{\Sigma}}_{\mathbf{C}\boldsymbol{\upsilon}}(\mathbf{W}^{(m)})\mathbf{s}} \\ \text{s.t.} & \|\mathbf{s}\|_2^2 = 1 \\ & |s(n)|^2 = \gamma, \quad n = 0, ..., N-1. \end{cases}$$

If we define

$$\text{SINR}^{(m)} = \text{SINR}\left(\mathbf{S}^{(m)}, \mathbf{W}^{(m)}\right), \tag{15}$$

where, $\left\{\left(\mathbf{S}^{(m)}, \mathbf{W}^{(m)}\right)\right\}$ represents a sequence of points generated by the proposed sequential optimization procedure. We establish the stopping condition for alternatives between $\mathbf{S}^{(m)}$ and $\mathbf{W}^{(m)}$ as:

$$|\text{SINR}^{(m)} - \text{SINR}^{(m-1)}| \leq \eta. \tag{16}$$

The proposed sequential process exhibits several intriguing characteristics, as outlined in the following proposition.

Proposition 1. *Assume that $\mathcal{P}_{\mathbf{w}}^{(m)}$ and $\mathcal{P}_{\mathbf{s}}^{(m)}$ are solvable, implying that each is feasible, bounded, and has an achievable optimal value. It can be shown that the sequence $\left\{\text{SINR}^{(m)}\right\}$ is monotonically increasing and converges to a finite value.*

Proof. See Appendix 7.2 ■

Given the similarity in optimization problems $\mathcal{P}_{\mathbf{w}}^{(m)}$ and $\mathcal{P}_{\mathbf{s}}^{(m)}$, we will present them in a unified manner using the same notation based on $\mathbf{x}$ to avoid repetition.

Consider the task of solving the optimization problem $\bar{\mathcal{P}}_1$:

$$\bar{\mathcal{P}}_1: \quad \begin{cases} \max\limits_{\mathbf{x}} \min\limits_{k\in\{1,2,...,K\}} & \dfrac{\mathbf{x}^\dagger \mathbf{A}_k \mathbf{x}}{\mathbf{x}^\dagger \mathbf{B} \mathbf{x}} \\ \text{s.t.} & \|\mathbf{x}\|_2^2 = 1. \\ & |x(n)|^2 = \gamma, \quad n = 0, ..., N-1. \end{cases}$$

Here, $\mathbf{x}$ denotes our continuous variable, while k serves as our discrete variable (based on our definition of the uncertainty set in Section 3, k refers to the k^{th} element of the uncertainty set $\mathcal{I}_{\phi_1}^{\phi_2}$). Setting $\gamma = 1$ transforms the optimization problem $\bar{\mathcal{P}}_1$ into $\mathcal{P}_{\mathbf{s}}$ for the unconstrained case and $\mathcal{P}_{\mathbf{w}}$ for both the unconstrained and constant modulus cases. Additionally, setting $\gamma = \frac{1}{N}$ converts it into $\mathcal{P}_{\mathbf{s}}$ for the constant modulus case.

To simplify our objective function from a fractional quadratic form to a quadratic one, we first define the vector $\mathbf{e}_n$ as the n^{th} standard basis vector, whose n-th element is one and all other elements are zero. As a result, the inequality constraint can be rewritten as follows:

$$\left|\mathbf{e}_n^\dagger \mathbf{x}\right|^2 = \gamma, \quad n = 0, ..., N-1. \tag{17}$$

Besides, we introduce the variable change $\mathbf{y}$ as $\mathbf{y} = \frac{\mathbf{B}^{\frac{1}{2}}\mathbf{x}}{\|\mathbf{B}^{\frac{1}{2}}\mathbf{x}\|_2}$, which because of the constraint $\|\mathbf{x}\|_2 = 1$, $\mathbf{y}$ based on $\mathbf{x}$ can be written as follows:

$$\mathbf{x} = \frac{\mathbf{B}^{-\frac{1}{2}}\mathbf{y}}{\|\mathbf{B}^{-\frac{1}{2}}\mathbf{y}\|_2}. \tag{18}$$

By substituting (17) and (18) into the optimization problem $\bar{\mathcal{P}}_1$, we arrive at the equivalent problem $\bar{\mathcal{P}}_2$:

$$\bar{\mathcal{P}}_2: \quad \begin{cases} \max\limits_{\mathbf{y}} \min\limits_{k\in\{1,2,...,K\}} & \mathbf{y}^\dagger \mathbf{C}_k \mathbf{y} \\ \text{s.t.} & \|\mathbf{y}\|_2^2 = 1, \\ & \mathbf{y}^\dagger \mathbf{D}_n \mathbf{y} = 0, \quad n = 0, ..., N-1, \end{cases}$$

where $\mathbf{C}_k = \mathbf{B}^{-\frac{1}{2}}\mathbf{A}_k\mathbf{B}^{-\frac{1}{2}}$ and $\mathbf{D}_n = \mathbf{B}^{-\frac{1}{2}}\mathbf{e}_n\mathbf{e}_n^\dagger\mathbf{B}^{-\frac{1}{2}} - \gamma\mathbf{B}^{-1}$. Although the reformulated problem $\bar{\mathcal{P}}_2$ no longer involves a fractional quadratic objective, it remains NP-hard as it is a quadratically constrained quadratic program (QCQP).

By introducing an auxiliary variable χ for the objective value (the epigraph formulation) and lifting the vector $\mathbf{y}$ to a rank-one matrix $\mathbf{Y} = \mathbf{y}\mathbf{y}^\dagger$, we reformulate $\bar{\mathcal{P}}_2$ as follows:

$$\bar{\mathcal{P}}_3 : \begin{cases} \max\limits_{\mathbf{Y},\chi} & \chi \\ \text{s.t.} & \text{tr}(\mathbf{C}_k\mathbf{Y}) \geq \chi, \quad k \in 1, 2, ..., K \\ & \text{tr}(\mathbf{Y}) = 1 \\ & \mathbf{Y} = \mathbf{Y}^\dagger \\ & \mathbf{Y} \succeq \mathbf{0} \\ & \text{rank}(\mathbf{Y}) = 1 \\ & \text{tr}(\mathbf{D}_n\mathbf{Y}) = 0, \quad n = 0, ..., N-1. \end{cases}$$

To address $\bar{\mathcal{P}}_3$, we perform a variable substitution $\mathbf{Y} = \mathbf{Z}$, enabling the application of the ADMM. Recently, numerous studies have focused on the convergence of ADMM for non-convex and non-smooth functions [51–60]. Although our problem seems non-convex at first glance, the convergence results in [55, 56] demonstrate that the optimization problem $\bar{\mathcal{P}}_3$ meets the conditions required to apply ADMM. In [55], the authors show that an inequality rank constraint, specifically $\text{Rank}(\mathbf{Y}) \leq r$ (where r is an upper bound on the rank), can be expressed as an indicator function:

$$\delta_{\mathcal{C}}(\mathbf{Y}) = \begin{cases} 0, & \text{if } \mathbf{Y} \in \mathcal{C} \\ +\infty, & \text{if } \mathbf{Y} \notin \mathcal{C} \end{cases}$$

for the rank-constrained set $\mathcal{C} = \{\mathbf{Y} \in \mathbb{R}^{m\times n} : \text{rank}(\mathbf{Y}) \leq r\}$. The authors proceed to validate the use of ADMM to decouple the rank constraint from the objective function (see Sections 3 and 4 of [55] for details). Given that our rank equality constraint is equivalent to $\text{rank}(\mathbf{Y}) \leq 1$, and based on the proof in [55], we are justified in applying ADMM, which allows us to separate the non-convex constraint $\text{rank}(\mathbf{Y}) = 1$ from

the other constraints, yielding:

$$\bar{\mathcal{P}}_4: \begin{cases} \max\limits_{\mathbf{Y},\chi,\mathbf{Z}} & \chi \\ \text{s.t.} & \text{tr}(\mathbf{C}_k\mathbf{Y}) \geq \chi, \quad k \in \{1,2,...,K\} \\ & \text{tr}(\mathbf{Y}) = 1 \\ & \mathbf{Y} = \mathbf{Y}^\dagger \\ & \mathbf{Y} \succeq \mathbf{0} \\ & \text{tr}(\mathbf{D}_n\mathbf{Y}) = 0, \quad n = 0,...,N-1. \\ & \mathbf{Y} = \mathbf{Z} \\ & \text{rank}(\mathbf{Z}) = 1. \end{cases}$$

Hence, the related augmented Lagrangian (AL) function takes the form:

$$\mathcal{L}_\rho(\mathbf{Y},\chi,\mathbf{Z},\mathbf{T}) = \chi - \langle \mathbf{T}, \mathbf{Y}-\mathbf{Z}\rangle - \frac{\rho}{2}\|\mathbf{Y}-\mathbf{Z}\|_F^2 \tag{19}$$

without directly associating other constraints with it. In (19), ρ represents the penalty parameter and $\mathbf{T}$ denotes the Lagrange multiplier. Following this, we outline the specific procedures for updating $\mathbf{Y}$, χ, $\mathbf{Z}$, and $\mathbf{T}$.

5.0.1. Updating $\mathbf{Y}$, χ

Regarding the update of $\mathbf{Y}$ and χ, while keeping the variables $\mathbf{Z}$ and $\mathbf{T}$ fixed, we have:

$$\bar{\mathcal{P}}_4^{\mathbf{Y},\chi}: \begin{cases} \max\limits_{\mathbf{Y},\chi} & \chi - \text{tr}(\mathbf{T}^\dagger\mathbf{Y}) + \rho\text{tr}(\mathbf{Z}^\dagger\mathbf{Y}) \\ \text{s.t.} & \text{tr}(\mathbf{C}_k\mathbf{Y}) \geq \chi, \quad k \in \{1,2,...,K\} \\ & \text{tr}(\mathbf{Y}) = 1 \\ & \mathbf{Y} = \mathbf{Y}^\dagger \\ & \mathbf{Y} \succeq \mathbf{0} \\ & \text{tr}(\mathbf{D}_n\mathbf{Y}) = 0, \quad n = 0,...,N-1. \end{cases}$$

It is obvious that $\tilde{\mathcal{P}}_4^{\mathbf{Y},\chi}$ is a convex SDP problem and can be efficiently solved using CVX [61].

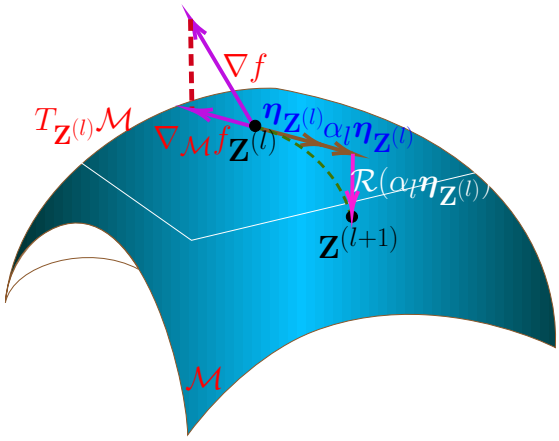

Figure 2: Geometric interpretations of Riemannian steepest descent (RSD)

5.0.2. Updating $\mathbf{Z}$

Concerning the update of $\mathbf{Z}$, we arrive at the following optimization problem:

$$\bar{\mathcal{P}}_4^{\mathbf{Z}}: \quad \begin{aligned} \min_{\mathbf{Z}} \quad & f(\mathbf{Z}) = \frac{\rho}{2}\|\mathbf{Z}\|_F^2 - \rho \mathrm{tr}(\mathbf{Y}^\dagger \mathbf{Z}) - \mathrm{tr}(\mathbf{T}^\dagger \mathbf{Z}) \\ \text{s.t.} \quad & \mathrm{rank}(\mathbf{Z}) = 1. \end{aligned}$$

With the analytical expression of $f(\mathbf{Z})$ available, we suggest a fixed-rank manifold-based method to tackle $\bar{\mathcal{P}}_4^{\mathbf{Z}}$. This approach, which utilizes iterative updates of the decomposition components of $\mathbf{Z}$ without factorization. The geometric structure of the manifold helps bypass certain saddle points and provides superior solutions to our problem. Essentially, the manifold acts as an extension of Euclidean space, but it can only be locally approximated by a linear space around a given point. The algorithm we develop is a variant of the steepest gradient descent algorithm, where geometric operations are performed to transition from Euclidean space to the manifold. To help understand this idea, we have shown a geometric interpretation in Fig. 2.

We treat the feasible region constrained by the fixed rank as our manifold. As a result, $\bar{\mathcal{P}}_4^{\mathbf{Z}}$ is viewed as an unconstrained optimization problem on the manifold defined as:

$$\mathcal{M}_k = \{\mathbf{Z} \in \mathbb{C}^{m\times n} : \mathrm{rank}(\mathbf{Z}) = k\}. \tag{20}$$

In an alternative description, if we want to represent our manifold based on the factorization $\mathbf{Z}$, we have [62, 63]:

$$\mathcal{M}_k = \{\mathbf{L}\mathbf{R}^\dagger : \mathbf{L} \in \mathbb{C}^{m\times k}, \mathbf{R} \in \mathbb{C}^{n\times k}\}. \tag{21}$$

This factorization is not unique because the group action

$$(\mathbf{L}, \mathbf{R}) \mapsto (\mathbf{L}\mathbf{M}^{-1}, \mathbf{R}\mathbf{M}^{\dagger}), \tag{22}$$

where $\mathbf{M} \in \mathrm{GL}(k) = \{\mathbf{M} \in \mathbb{C}^{k\times k} : \det(\mathbf{M}) \neq 0\}$, leaves the original matrix $\mathbf{Z}$ unchanged. This mapping allows us to identify the search space of interest with the quotient space

$$\mathcal{F}(k, m, n) \cong (\mathbb{C}^{m\times k} \times \mathbb{C}^{n\times k})/\mathrm{GL}(k), \tag{23}$$

which represents the set of equivalence classes

$$[(\mathbf{L}, \mathbf{R})] = \{(\mathbf{L}\mathbf{M}^{-1}, \mathbf{R}\mathbf{M}^{\dagger}) : \mathbf{M} \in \mathrm{GL}(k)\}. \tag{24}$$

The manifold $\mathcal{M}_k$ is equipped with a metric $g(\boldsymbol{\xi}_{\mathbf{Z}}, \boldsymbol{\zeta}_{\mathbf{Z}})$, which represents an inner product between elements $\boldsymbol{\xi}_{\mathbf{Z}}$ and $\boldsymbol{\zeta}_{\mathbf{Z}}$ of the tangent space $T_{\mathbf{Z}}\mathcal{M}$ at the point $\mathbf{Z}$. The Riemannian gradient at $\mathbf{Z}$ is determined based on the selected metric. It is defined as the unique element $\nabla_{\mathcal{M}} f(\mathbf{Z}) \in T_{\mathbf{Z}}\mathcal{M}$ that fulfills the condition

$$\mathcal{D}f(\mathbf{Z})[\boldsymbol{\xi}_{\mathbf{Z}}] = g(\nabla_{\mathcal{M}} f(\mathbf{Z}), \boldsymbol{\xi}_{\mathbf{Z}}), \quad \forall \boldsymbol{\xi}_{\mathbf{Z}} \in T_{\mathbf{Z}}\mathcal{M}. \tag{25}$$

Here, $\mathcal{D}f(\mathbf{Z})[\boldsymbol{\xi}_{\mathbf{Z}}]$ denotes the directional derivative of $f(\mathbf{Z})$ in the direction of $\boldsymbol{\xi}_{\mathbf{Z}}$.

Essentially, a quotient manifold is comprised of equivalence classes. For instance, the Grassmann manifold $\mathrm{Gr}(r, d)$ represents the set of r-dimensional subspaces in $\mathbb{R}^d$, seen as a collection of r-dimensional orthogonal frames that cannot be aligned by a rotation. In the case of a quotient manifold $\mathcal{M} = \bar{\mathcal{M}}/\sim$, where $\bar{\mathcal{M}}$ is the total space and $\sim$ is the equivalence relation defining the quotient, a tangent vector $\xi_{[\mathbf{Z}]} \in T_{\mathbf{Z}}\mathcal{M}$ at $[\mathbf{Z}]$ is limited to directions that do not cause a shift along the set of equivalence classes $[\mathbf{Z}]$. In this paper, we adopt the following Riemannian metric:

$$\begin{aligned} &g\left((\bar{\boldsymbol{\xi}}_{\mathbf{L}}, \bar{\boldsymbol{\xi}}_{\mathbf{R}}), (\bar{\boldsymbol{\zeta}}_{\mathbf{L}}, \bar{\boldsymbol{\zeta}}_{\mathbf{R}})\right) \\ &= \mathrm{Tr}\left((\mathbf{L}^{\dagger}\mathbf{L})^{-1}\bar{\boldsymbol{\xi}}_{\mathbf{L}}^{\dagger}\bar{\boldsymbol{\zeta}}_{\mathbf{L}}\right) + \mathrm{Tr}\left((\mathbf{R}^{\dagger}\mathbf{R})^{-1}\bar{\boldsymbol{\xi}}_{\mathbf{R}}^{\dagger}\bar{\boldsymbol{\zeta}}_{\mathbf{R}}\right), \end{aligned} \tag{26}$$

which remains unchanged across the set of equivalence classes [64]. Utilizing this metric and definition

(25), the Riemannian gradient $\nabla_{\mathcal{M}} f(\mathbf{Z})$ is denoted as:

$$\nabla_{\mathcal{M}} f(\mathbf{L}, \mathbf{R}) = \left(\nabla^{\mathbf{L}} f(\mathbf{Z}) \mathbf{L}^{\dagger} \mathbf{L}, \nabla^{\mathbf{R}} f(\mathbf{Z}) \mathbf{R}^{\dagger} \mathbf{R}\right), \tag{27}$$

where $\nabla^{\mathbf{L}} f(\mathbf{Z})$ and $\nabla^{\mathbf{R}} f(\mathbf{Z})$ are the Euclidean gradients of $f(\mathbf{Z})$ with respect to $\mathbf{L}$ and $\mathbf{R}$, respectively.

Armed with the Riemannian gradient $\nabla_{\mathcal{M}} f$, manifold optimization smoothly adopts various techniques developed for Euclidean spaces. By using the negative Riemannian gradients with respect to $\mathbf{L}$ and $\mathbf{R}$ as our search directions, we iteratively update $\mathbf{L}$ and $\mathbf{R}$. This approach is what we refer to as fixed-rank Riemannian steepest descent (FR-RSD):

$$\mathbf{L}^{(l)} = \mathbf{L}^{(l-1)} - \alpha^{(l)} \nabla^{\mathbf{L}} f(\mathbf{Z}) \mathbf{L}^{(l-1)^{\dagger}} \mathbf{L}^{(l-1)}, \tag{28}$$

$$\mathbf{R}^{(l)} = \mathbf{R}^{(l-1)} - \alpha^{(l)} \nabla^{\mathbf{R}} f(\mathbf{Z}) \mathbf{R}^{(l-1)^{\dagger}} \mathbf{R}^{(l-1)}. \tag{29}$$

In the FR-RSD algorithm, ensuring a decrease in $f(\mathbf{Z})$ with each iteration is vital. To achieve this, we employ the Armijo line-search method [65] to determine the step size $\alpha^{(l)}$. For a summary of our proposed method, refer to **Algorithm 1**.

5.0.3. Updating $\mathbf{T}$

In updating our Lagrange multiplier matrix $\mathbf{T}_i$, we use the results from updating $\mathbf{X}$ and $\mathbf{Z}$, denoted as $\mathbf{X}_i$ and $\mathbf{Z}_i$, respectively. This gives us:

$$\mathbf{T}_{i+1} = \mathbf{T}_i + \rho(\mathbf{X}_i - \mathbf{Z}_i). \tag{30}$$

According to the inner ADMM process we discussed, we need to continue iterating through $\mathbf{X}_i$, $\mathbf{Z}_i$, and $\mathbf{T}_i$ until the following stopping criterion is satisfied:

$$\|\mathbf{X}_i - \mathbf{Z}_i\|_F \leq \eta_{\text{ADMM}}. \tag{31}$$

Afterward, the optimal value $\mathbf{x}_{opt}$ of $\bar{\mathcal{P}}_1^q$ is equal to the factor $\mathbf{L}$ as defined in (21). For a summary of the proposed method, which we call the alternating direction method of multipliers with semidefinite programming and fixed-rank steepest descent (ADMM-SFRS) method, please see **Algorithm 2**.

Algorithm 1: FR-RSD Method

Require: Function $f : \mathbb{C}^{m\times k} \times \mathbb{C}^{n\times k} \to \mathbb{C}$, an initial point for $\mathbf{L}^{(0)} \in \mathbb{C}^{m\times k}$, $\mathbf{R}^{(0)} \in \mathbb{C}^{n\times k}$, and tolerance parameter $\epsilon > 0$.
Ensure: A solution $\mathbf{Z}^*$ to $\tilde{\mathcal{P}}_5^{\mathbf{Z}}$
Set: $l = 0$, $\mathbf{Z}^{(0)} = \mathbf{L}^{(0)}\mathbf{R}^{(0)\dagger}$
Compute Riemannian gradient $\nabla_{\mathcal{M}} f(\mathbf{Z}^{(l)})$ from (27)
While $\|\nabla_{\mathcal{M}} f(\mathbf{Z}^{(l)})\| > \epsilon$ **do**

1. $l = l + 1$
2. Use Armijo line search to update $\alpha^{(l)}$:
   (a) Initialize $\psi(0) = \gamma > 0$, $\beta, \delta \in (0, 1)$, $t = 0$
   (b) **Repeat**
      i. $\psi(t) = \beta^{(t)}\gamma$
      ii. $\mathbf{L}^{(l)} = \mathbf{L}^{(l-1)} - \psi(t)\nabla^{\mathbf{L}} f(\mathbf{Z})\mathbf{L}^{(l-1)\dagger}\mathbf{L}^{(l-1)}$
      iii. $\mathbf{R}^{(l)} = \mathbf{R}^{(l-1)} - \psi(t)\nabla^{\mathbf{R}} f(\mathbf{Z})\mathbf{R}^{(l-1)\dagger}\mathbf{R}^{(l-1)}$
      iv. $\mathbf{Z}^{(l)} = \mathbf{L}^{(l)}\mathbf{R}^{(l)\dagger}$
      v. $t = t + 1$
   Until $\frac{f(\mathbf{Z}^{(l)}) - f(\mathbf{Z}^{(l-1)})}{\|\nabla_{\mathcal{M}} f(\mathbf{Z}^{(l-1)})\|_F^2} \leq -\delta\psi(t)$
3. $\alpha^{(l)} = \psi(t)$
4. $\mathbf{L}^{(l)} = \mathbf{L}^{(l-1)} - \alpha^{(l)}\nabla^{\mathbf{L}} f(\mathbf{Z})\mathbf{L}^{(l-1)\dagger}\mathbf{L}^{(l-1)}$
5. $\mathbf{R}^{(l)} = \mathbf{R}^{(l-1)} - \alpha^{(l)}\nabla^{\mathbf{R}} f(\mathbf{Z})\mathbf{R}^{(l-1)\dagger}\mathbf{R}^{(l-1)}$
6. Compute Riemannian gradient $\nabla_{\mathcal{M}} f(\mathbf{Z}^{(l)})$ from (27)

End While

5.1. Computational Complexity of ADMM-SFRS

In this paper, solving each of the subproblems $\mathcal{P}_{\mathbf{w}}^{(m)}$ and $\mathcal{P}_{\mathbf{s}}^{(m)}$ with the proposed ADMM-SFRS method involves a decomposition into an SDP component and a fixed-rank optimization component. Consequently, the dominant computational cost is driven by the SDP solver. The SDP component of the receive filter optimization, $\mathcal{P}_{\mathbf{w}}^{(m)}$, has a complexity of $O(N^{4.5})$ [6]. Similarly, the SDP component of the transmit signal optimization, $\mathcal{P}_{\mathbf{s}}^{(m)}$, has a complexity of $O(M^{4.5})$. Furthermore, as detailed in Algorithm 1, the complexity of solving the fixed-rank part of $\mathcal{P}_{\mathbf{w}}^{(m)}$ is $O(M)$, and for $\mathcal{P}_{\mathbf{s}}^{(m)}$, it is $O(N)$ due to the rank-1 constraint. Since these linear complexities are significantly lower than the polynomial complexity of the SDP steps, they do not dominate the overall computation. Therefore, the total complexity for solving $\mathcal{P}_{\mathbf{w}}^{(m)}$ and $\mathcal{P}_{\mathbf{s}}^{(m)}$ per iteration is effectively determined by the SDP solver, resulting in complexities of $O(N^{4.5})$ and $O(M^{4.5})$, respectively.

To the best of our knowledge, existing methods for this worst-case optimization problem such as [5–7] also rely on SDP and do not hold a computational advantage over our proposed algorithm. A key distinction is that many of them utilize problem relaxations, which cannot guarantee a high-quality final

Algorithm 2: ADMM-SFRS

Require: $\mathbf{A}_k = 0$, $\mathbf{B}$, λ, $\mathbf{x}^(0)$, η_{ADMM}
Ensure: A solution $\mathbf{x}_{\text{opt}}$ for $\bar{\mathcal{P}}_1$
Set: $i = 0$, $\mathbf{X}^{(0)} = \mathbf{x}^{(0)}\mathbf{x}^{(0)\dagger}$;
Repeat

1. $i = i + 1$
2. Solve $\bar{\mathcal{P}}_4^{\mathbf{X},\chi}$ finding an optimal value $\mathbf{X}^{(i)}$
3. Solve $\bar{\mathcal{P}}_4^{\mathbf{Z}}$ based on **Algorithm 1** finding optimal values $\mathbf{Z}^{(i)}$, $\mathbf{L}^{(i)}$
4. Update $\mathbf{T}^{(i)}$ based on (30).

Until $\|\mathbf{X}^{(i)} - \mathbf{Z}^{(i)}\|_F \leq \eta_{\text{ADMM}}$
Output: $\mathbf{x}_{\text{opt}} = \mathbf{L}^{(i)}$

solution. In contrast, our method addresses the problem directly, ensuring a more reliable outcome.

6. Numerical Results

In this section, we evaluate the performance of the proposed technique across various scenarios using the available TIR information, described through the uncertainty set. We focus on an S-band radar with a rectangular subpulse duration of 6.67 ns and an operating frequency of $f_c = 3$ GHz, which provides a range resolution of approximately 1 meter. To model the TIR of an extended target, we simulate radar backscattering data for three different targets using the simulation software mentioned in [66, 67]. The targets are characterized by their dimensions as follows: the Tornado has a length of 16.72 meters and a width of 13.91 meters, while the F15 has a length of 19.43 meters and a width of 13.05 meters. Based on the targets' dimensions and the radar's range resolution, we set the TIR support interval to $Q = 17$.

Now, we aim to describe the statistical properties of the clutter environment and noise. We consider a homogeneous clutter environment where the elements of the covariance matrix follow an exponential form:

$$R_c(n, n') = \sigma_c^2 r^{-|n-n'|}, \quad (n, n') \in \{1, ..., M + N\}^2. \tag{32}$$

Here, we set $\sigma_c^2 = 10$ and $r = 0.8$ [6]. Furthermore, we chose the initial value of the transmitted waveform to be a sequence with linear frequency modulation (LFM) to fulfill condition $\mathcal{P}$ concerning the signal energy:

$$s_0(n) = \frac{1}{\sqrt{N}} e^{j\pi \frac{n^2}{2N}}, n = 0, 1, ..., N - 1. \tag{33}$$

As to the noise, we suppose a discrete white noise with variance $\sigma_{\boldsymbol{v}}^2 = 1$. Regarding the stopping criteria

for the devised methods, we set $\rho = 5$, $\eta_{\text{ADMM}} = 10^{-4}$, and $\eta = 10^{-4}$. Additionally, for the FR-RSD algorithm, we consider a tolerance parameter of $\epsilon = 10^{-4}$.

Now, our goal is to assess the effectiveness of our proposed method in jointly designing the transmit signal and the receive filter for both unconstrained and constant modulus situations. We will consider three distinct scenarios, as outlined below:

1. Examination of various TAA uncertainty sets for a specific target.
2. Investigation into how different types of targets behave under a TAA uncertainty set.
3. Convergence speed determined by the number of iterations.

Regarding the consideration of the uncertainty set, we set the TAA sampling step of $\mathcal{I}_{\phi_1}^{\phi_2}$ to 0.1 degrees in our simulations. For each TAA $k\Delta\theta$ within this uncertainty set, we compute the actual TIR using the toolbox referenced in [66, 67].

To showcase the effectiveness of our method, we evaluate the optimized SINR achieved by our approach in comparison with other waveform–filter design techniques adapted from their original applications to the extended-target scenario:

1. A simplified version of the unconstrained design technique proposed in [1], which assumes a known TIR and is tailored for the SISO case.
2. The method from [2], originally developed for MIMO-ISAC systems; when applied to extended targets, it likewise assumes a known TIR and employs randomization strategies to generate the waveform–filter pair.
3. The manifold-based approach from [3, 4], which presumes perfect TIR knowledge and incorporates a constant-modulus constraint, defining a complex-circle manifold and using Riemannian conjugate-gradient descent for waveform–filter design.
4. The robust design methods from [5–7], which account for TIR uncertainty and employ randomization to synthesize the waveform–filter pair under both unconstrained and constant-modulus settings.

In our paper, we denote our proposed method as ADMM-SFRS (U) for the unconstrained scenario and as ADMM-SFRS (CM) for the constant modulus scenario.

6.1. The Optimal SINR Obtained for Different TAAs

In Fig. 3, we plot the worst-case SINR, denoted $\min_{\theta\in\mathcal{I}_{-\theta^\circ}^{\theta^\circ}} \text{SINR}^{(m)}(\theta)$, against the iteration index m for target F15 under the uncertainty sets $\mathcal{I}_{-4.5^\circ}^{4.5^\circ}$ and $\mathcal{I}_{-10.5^\circ}^{10.5^\circ}$. Because some of our competitors, such as

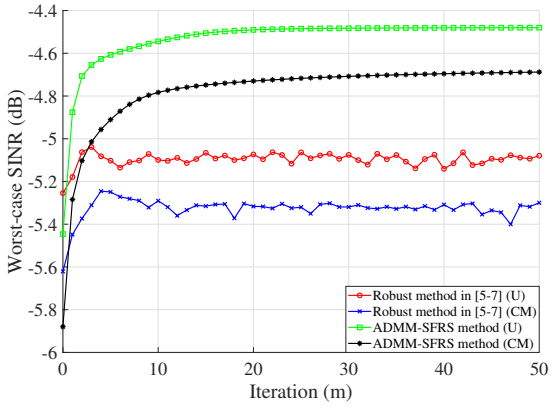

(a)

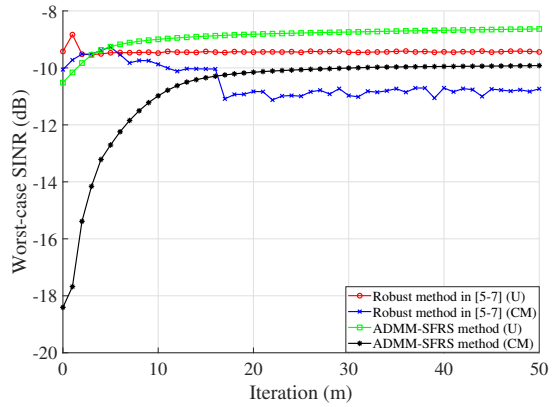

(b)

Figure 3: Plotting $\mathrm{SINR}^{(m)}$ versus the iterations, over different uncertainty sets for F15: (a) $\mathcal{I}_{-4.5^\circ}^{4.5^\circ}$ and (b) $\mathcal{I}_{-10.5^\circ}^{10.5^\circ}$.

[1–4], do not address the worst-case problem, their performance curves are not directly comparable in this setting.

The plots indicate that, as the uncertainty set expands, the optimized worst-case SINR decreases. This behavior aligns with the principle that for two uncertainty sets $\mathcal{I}_1 \subseteq \mathcal{I}_2$, $\min_{\theta\in\mathcal{I}_2} \mathrm{SINR}_\theta(s,w) \leq \min_{\theta\in\mathcal{I}_1} \mathrm{SINR}_\theta(s,w)$. Therefore, solving the problem over a larger uncertainty set yields a worst-case SINR value that is less than or equal to that obtained with a smaller set. Furthermore, Fig. 3 shows that ADMM-SFRS (U) and ADMM-SFRS (CM) achieve superior worst-case SINR values compared to the robust method [5–7] in both the unconstrained and constant-modulus scenarios. To ensure a fair comparison in accuracy, we randomly selected 10,000 samples for the randomization part. We also note that in [6], the authors plotted a relaxed (rank-dropped) version of the worst-case SINR problem versus iteration, whereas in this paper we plot the original worst-case SINR.

Beyond analyzing the worst-case SINR value, it is also important to evaluate the performance of the synthesized robust waveform–filter pair across all TAA points in the uncertainty set (see Figs. 4 and 5). To facilitate a better comparison between the ADMM-SFRS method (in both unconstrained and constant-modulus designs) and its competitors, we have divided the plots into two parts.

In Fig. 4, we compare ADMM-SFRS (U) and (CM) with the methods that assume a known TIR. As mentioned earlier, these methods do not account for worst-case optimization; they focus exclusively on maximizing SINR within the uncertainty set $\mathcal{I}_{0^\circ}^{0^\circ}$.

In Fig. 5, we compare our proposed method with the robust methods in both the unconstrained and constant-modulus scenarios from [5–7]. This comparison is more equitable because both our proposed method and the robust methods from [6] aim to design the transmit waveform and receive filter based on the worst-case SINR over the predefined uncertainty set. The uncertainty sets considered for comparison are $\mathcal{I}_{-4.5^\circ}^{4.5^\circ}$, $\mathcal{I}_{-7.5^\circ}^{7.5^\circ}$, and $\mathcal{I}_{-10.5^\circ}^{10.5^\circ}$.

As discussed earlier, the plots in Fig. 5 highlight that increasing the size of the TAA uncertainty set results in lower worst-case SINR values. Furthermore, the results from Figs. 4 and 5 reveal that the ADMM-SFRS method achieves higher optimized minima (the minimum SINR values of each method within the figures have been magnified for clarity) and more consistent SINR values compared to the nominal design and its primary competitor, the robust design proposed by [6]. In other words, whether in an unconstrained or constant-modulus scenario, the ADMM-SFRS method exhibits more robust behavior, avoids extreme fluctuations, and demonstrates smoother performance.

6.2. Uncertainty Set for Another Target Type

In this subsection, we examine the performance of the ADMM-SFRS method for Tornado as another target type (see Figs. 6 and 7), in a manner similar to our analysis of the F15 target (Figs. 4 and 5).

As observed, the methods of [1], the manifold-based approaches of [3, 4], and the nominal method of [2] exhibit the poorest performance due to their reliance on the matched scenario $\mathcal{I}_{0^\circ}^{0^\circ}$, resulting in low robustness. In contrast, the ADMM-SFRS method demonstrates superior performance in both unconstrained and constant-modulus scenarios, achieving higher minimum SINR values and a flatter response within the uncertainty sets compared to the UR and CMR methods.

The next-best performance is delivered by the robust methods of [5–7] in both unconstrained and constant-modulus scenarios. Although the robust methods of [5–7] offer robust SINR, they remain outperformed by ADMM-SFRS in terms of smoothness and minimum SINR level.

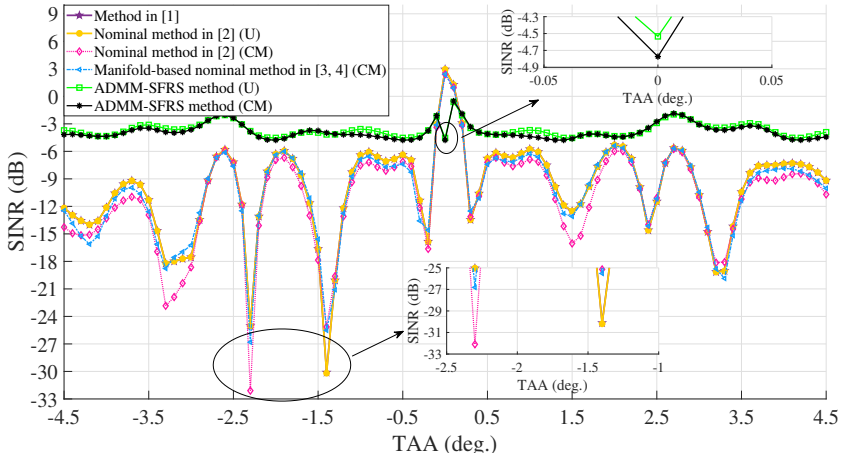

(a)

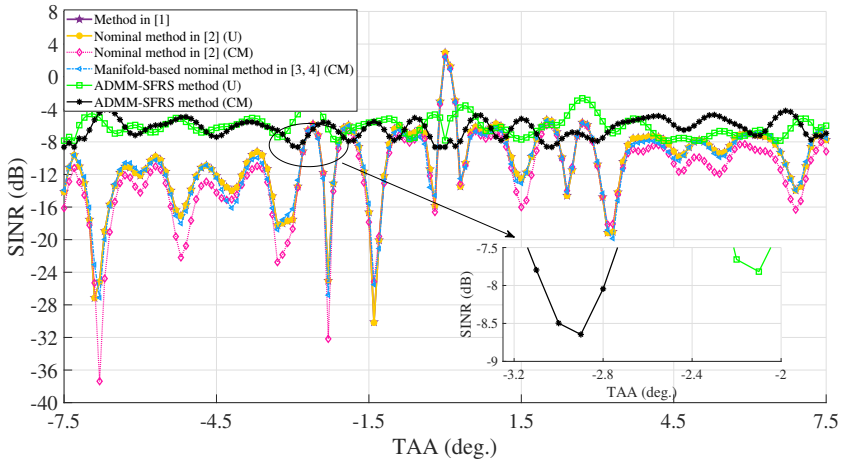

(b)

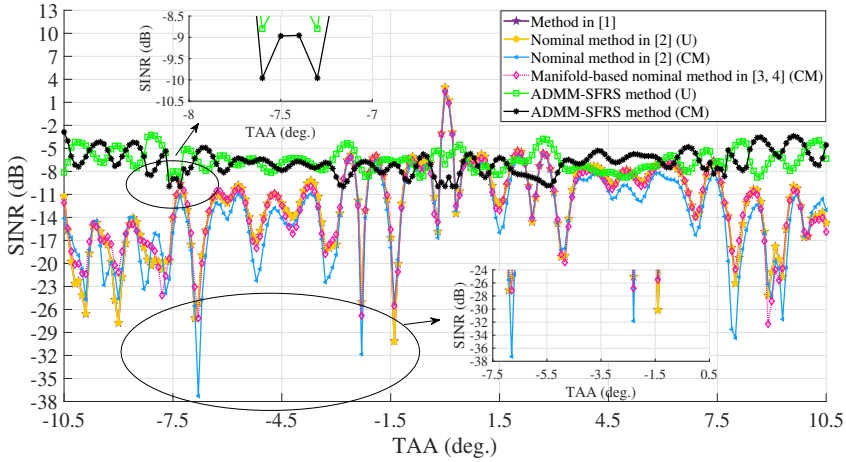

(c)

Figure 4: SINR versus TAA, over different uncertainty sets for F15: (a) $\mathcal{I}_{-4.5^\circ}^{4.5^\circ}$, (b) $\mathcal{I}_{-7.5^\circ}^{7.5^\circ}$, and (c) $\mathcal{I}_{-10.5^\circ}^{10.5^\circ}$.

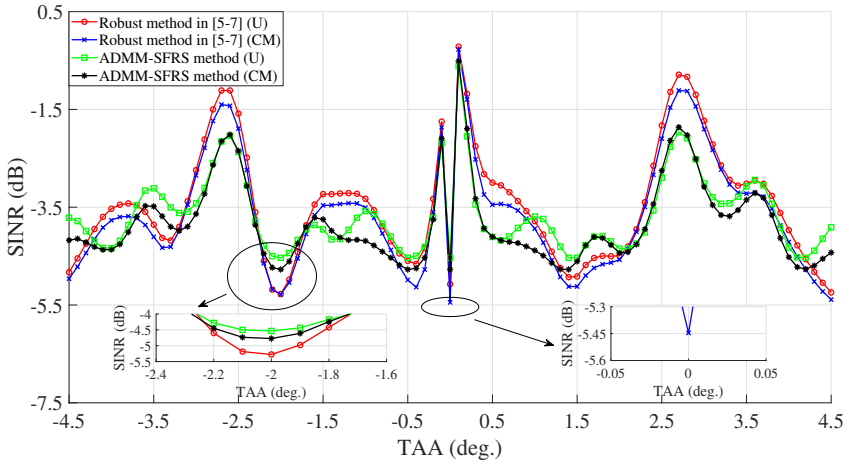

(a)

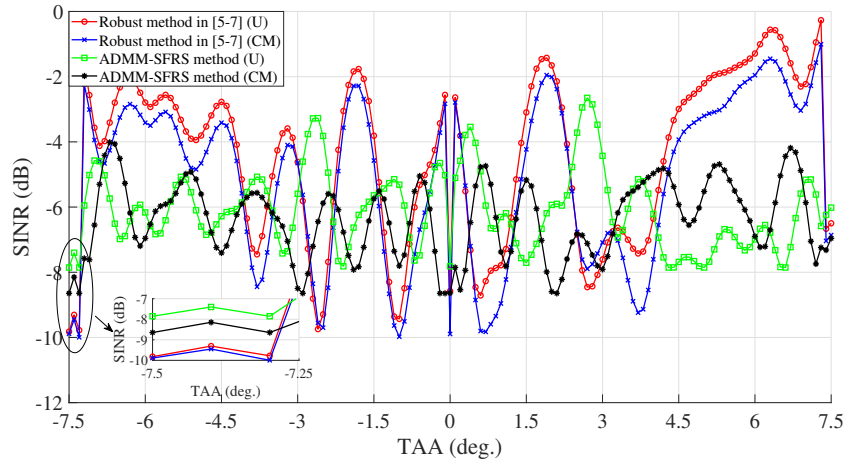

(b)

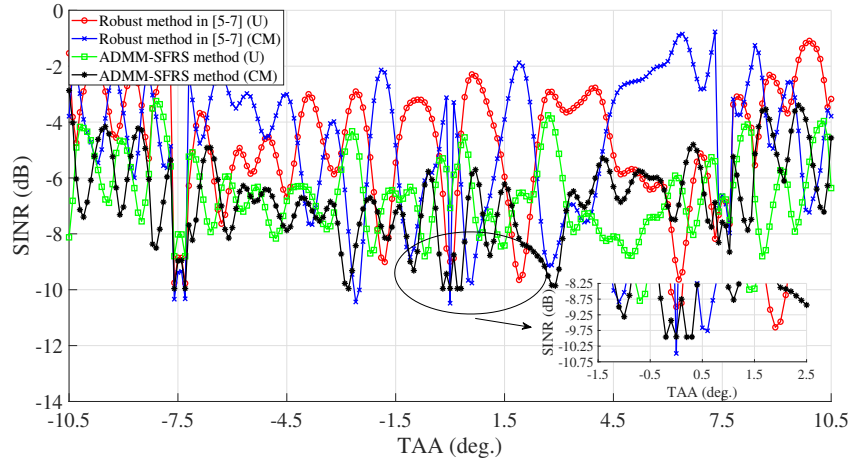

(c)

Figure 5: SINR versus TAA, over different uncertainty sets for F15: (a) $\mathcal{I}_{-4.5^\circ}^{4.5^\circ}$, (b) $\mathcal{I}_{-7.5^\circ}^{7.5^\circ}$, and (c) $\mathcal{I}_{-10.5^\circ}^{10.5^\circ}$.

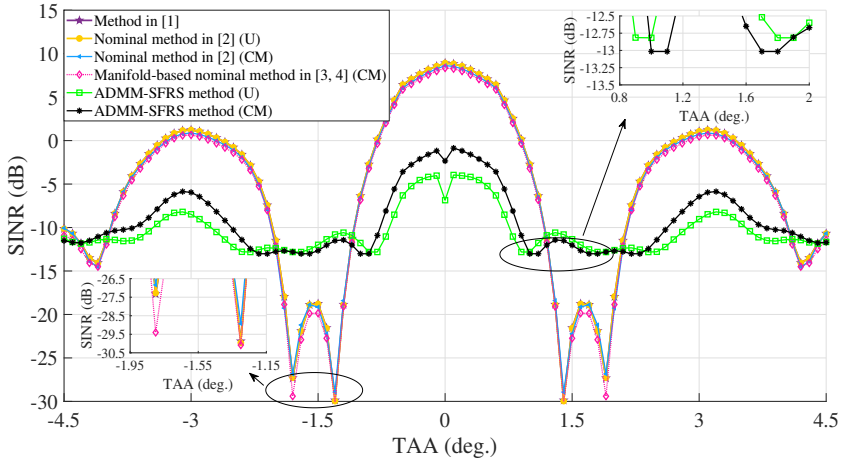

(a)

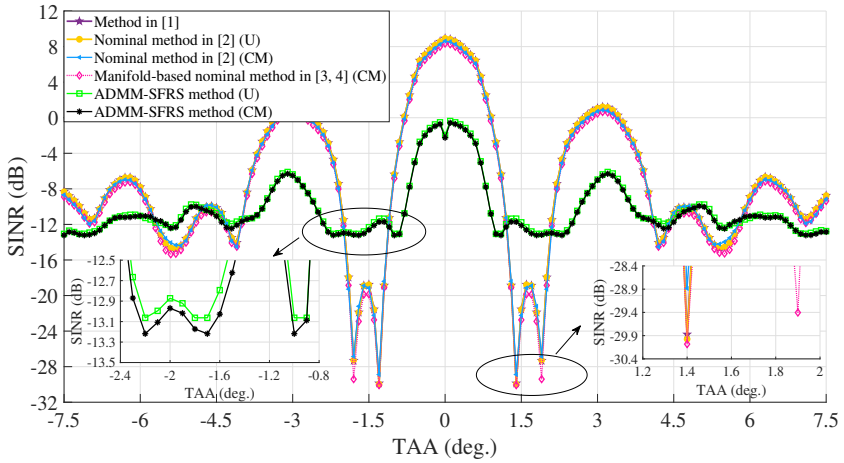

(b)

Figure 6: SINR versus TAA for the Tornado over: (a) $\mathcal{I}_{-4.5^\circ}^{4.5^\circ}$, (b) $\mathcal{I}_{-7.5^\circ}^{7.5^\circ}$

.

6.3. Analysis of Iteration Execution

We now examine the convergence speed of our proposed approach, measured by iteration count, against the robust methods of [5–7]. As shown in Fig. 3, ADMM-SFRS converges in fewer iterations than these robust methods in both unconstrained and constant-modulus scenarios. This advantage is particularly evident in Fig. 3(a).

These results further confirm the convergence properties of ADMM-SFRS under both unconstrained and constant-modulus constraints.

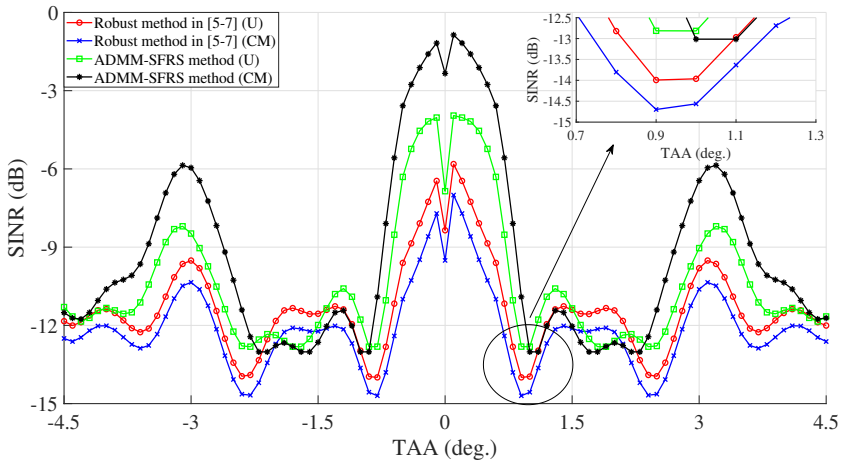

(a)

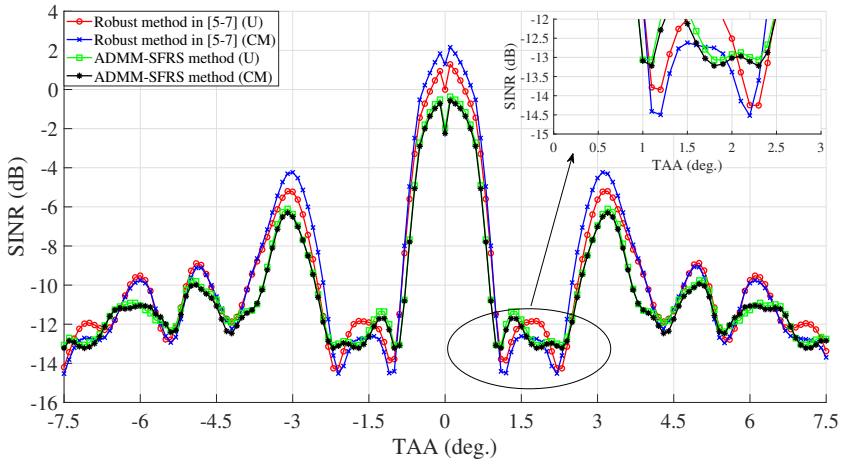

(b)

Figure 7: SINR versus TAA for the Tornado over: (a) $\mathcal{I}_{-4.5^\circ}^{4.5^\circ}$, (b) $\mathcal{I}_{-7.5^\circ}^{7.5^\circ}$

.

Table 2: Runtime performance (in seconds) across different uncertainty sets and target types.

Category	**Algorithm**	$\mathcal{I}_{-4.5^\circ}^{4.5^\circ}$ (F15)	$\mathcal{I}_{-7.5^\circ}^{7.5^\circ}$ (F15)	$\mathcal{I}_{-10.5^\circ}^{10.5^\circ}$ (F15)	$\mathcal{I}_{-4.5^\circ}^{4.5^\circ}$ (Tornado)	$\mathcal{I}_{-7.5^\circ}^{7.5^\circ}$ (Tornado)
Constant Energy	Robust method in [5–7] (U)	291.433	463.253	623.226	297.291	470.447
	ADMM-SFRS (U)	217.930073	286.092	353.250	182.671	234.666
Constant Modulus	Robust method in [5–7] (CM)	295.939	458.142	627.367	297.501	463.516
	ADMM-SFRS (CM)	225.671	299.209	369.101	182.847	337.387

6.4. Execution Time

To account for computational complexity, we also evaluate each method based on its execution time. Table 2 reports the convergence times (in seconds) of our ADMM-SFRS approach compared to the robust methods of [5–7] under both unconstrained and constant-modulus scenarios. The ADMM-SFRS method exhibits superior runtime performance relative to the robust designs of [5–7]. We omit runtimes for the methods of [1], the manifold-based techniques of [3, 4], and the nominal method of [2], since these approaches only consider the matched scenario ($\mathcal{I}_{0^\circ}^{0^\circ}$) and do not address the worst-case optimization problem.

7. Conclusion

In this paper, we addressed the problem of jointly designing the transmit waveform and receive filter for extended targets in the presence of signal-dependent interference. To ensure practical feasibility and performance stability, we formulated a worst-case optimization problem that accounts for TIR uncertainty while strictly enforcing a constant modulus constraint on the transmit code. Our proposed design methodology employed a sequential optimization process. We utilized the ADMM to decompose the complex design problem into two more manageable sub-problems: an SDP problem and a non-convex problem characterized by a fixed-rank matrix constraint. For the latter, we proposed a Riemannian steepest descent (RSD) algorithm that operated on the manifold of fixed-rank matrices to effectively navigate the non-convex landscape.

Numerical results explicitly validate the efficacy of this approach, highlighting several key takeaways. First, the proposed method exhibits superior robustness compared to nominal designs, maintaining high SINR levels even under significant TIR mismatches. Second, our analysis confirms that ADMM-SFRS outperforms existing robust techniques based on semidefinite relaxation and randomization, delivering higher output SINR by avoiding relaxation losses. Third, the computational evaluation demonstrates a significant advantage in efficiency; the proposed algorithm converges with fewer iterations and reduced runtime compared to state-of-the-art baselines. These findings establish ADMM-SFRS as a powerful and practical framework for modern radar systems operating in uncertain and clutter-rich environments.

Appendix

7.1. The proof of the SINR formulation

Proof. To prove how we arrive at the numerators in (10), consider the following:

$$\begin{aligned}\left|\mathbf{w}^{\dagger}\mathbf{H}_{\theta}\mathbf{s}\right|^{2} &= \mathbf{w}^{\dagger}\mathbf{H}_{\theta}\mathbf{s}\mathbf{s}^{\dagger}\mathbf{H}_{\theta}{}^{\dagger}\mathbf{w} = \mathbf{w}^{\dagger}\Gamma(\mathbf{H}_{\theta},\mathbf{s})\mathbf{w} \\ &= \mathbf{s}^{\dagger}\mathbf{H}_{\theta}{}^{\dagger}\mathbf{w}\mathbf{w}^{\dagger}\mathbf{H}_{\theta}\mathbf{s} = \mathbf{s}^{\dagger}\bar{\mathbf{\Gamma}}(\mathbf{H}_{\theta},\mathbf{w})\mathbf{s}. \end{aligned} \tag{34}$$

In order to prove the denominator of (10), we simplify the denominator of (8) as follows:

$$\begin{aligned}\mathbb{E}[\left|\mathbf{w}^{\dagger}\mathbf{C}\mathbf{s}\right|^{2}] + \mathbb{E}[\left|\mathbf{w}^{\dagger}\boldsymbol{\upsilon}\right|^{2}] &= \mathbf{w}^{\dagger}\mathbb{E}[\mathbf{C}\mathbf{s}\mathbf{s}^{\dagger}\mathbf{C}^{\dagger}]\mathbf{w} + \mathbf{w}^{\dagger}\mathbb{E}[\boldsymbol{\upsilon}^{\dagger}\boldsymbol{\upsilon}]\mathbf{w} \\ &= \mathbf{w}^{\dagger}\mathbb{E}[\mathbf{C}\mathbf{s}\mathbf{s}^{\dagger}\mathbf{C}^{\dagger}]\mathbf{w} + \sigma_{\boldsymbol{\upsilon}}^{2}\mathbf{w}^{\dagger}\mathbf{w}\mathbf{I} \\ &= \mathbf{w}^{\dagger}\mathbf{\Sigma}_{\mathbf{C}\boldsymbol{\upsilon}}(\mathbf{s})\mathbf{w}. \end{aligned} \tag{35}$$

Considering the energy constraint $\|\mathbf{s}\|_2^2 = 1$, the denominator of (8) becomes:

$$\begin{aligned}\mathbb{E}[\left|\mathbf{w}^{\dagger}\mathbf{C}\mathbf{s}\right|^{2}] + \mathbb{E}[\left|\mathbf{w}^{\dagger}\boldsymbol{\upsilon}\right|^{2}] &= \mathbf{s}^{\dagger}\mathbb{E}[\mathbf{C}\mathbf{w}\mathbf{w}^{\dagger}\mathbf{C}^{\dagger}]\mathbf{s} + \mathbf{w}^{\dagger}\mathbb{E}[\boldsymbol{\upsilon}^{\dagger}\boldsymbol{\upsilon}]\mathbf{w} \\ &= \mathbf{s}^{\dagger}\mathbb{E}[\mathbf{C}\mathbf{w}\mathbf{w}^{\dagger}\mathbf{C}^{\dagger}]\mathbf{s} + \sigma_{\boldsymbol{\upsilon}}^{2}\mathrm{tr}(\mathbf{w}\mathbf{w}^{\dagger})\mathbf{I} \\ &= \mathbf{s}^{\dagger}\bar{\mathbf{\Sigma}}_{\mathbf{C}\boldsymbol{\upsilon}}(\mathbf{w})\mathbf{s}. \end{aligned} \tag{36}$$

■

7.2. The Proof of Proposition 1

Proof. Firstly, we demonstrate that the sequence $\left\{\mathrm{SINR}^{(m)}\right\}$ is monotonically increasing, meaning $\mathrm{SINR}^{(m)} \leq \mathrm{SINR}^{(m+1)}$. To show this, we consider:

$$\begin{aligned}\mathrm{SINR}^{(m)} &= \min_{\theta\in\mathcal{I}} \frac{\mathrm{tr}\left(\mathbf{\Gamma}\left(\mathbf{H}_{\theta},\mathbf{S}^{(m)}\right)\mathbf{W}^{(m)}\right)}{\mathrm{tr}\left(\mathbf{\Sigma}_{cv}\left(\mathbf{S}^{(m)}\right)\mathbf{W}^{(m)}\right)} \leq v\left(\mathcal{P}_{\mathbf{w}}^{(m+1)}\right) \\ &= \min_{\theta\in\mathcal{I}} \frac{\mathrm{tr}\left(\bar{\mathbf{\Gamma}}\left(\mathbf{H}_{\theta},\mathbf{W}^{(m+1)}\right)\mathbf{S}^{(m)}\right)}{\mathrm{tr}\left(\bar{\mathbf{\Sigma}}_{cv}\left(\mathbf{W}^{(m+1)}\right)\mathbf{S}^{(m)}\right)} \leq v\left(\mathcal{P}_{\mathbf{s}}^{(m+1)}\right) \\ &= \mathrm{SINR}^{(m+1)}. \end{aligned}$$

Secondly, we need to show that the objective function is bounded above. We start with:

$$\begin{aligned}
\mathrm{SINR}^{(m)} &= \min_{\theta\in\mathcal{I}} \frac{\mathrm{tr}\left(\bar{\mathbf{\Gamma}}\left(\mathbf{H}_\theta, \mathbf{W}^{(m)}\right)\mathbf{S}^{(m)}\right)}{\mathrm{tr}\left(\bar{\mathbf{\Sigma}}_{cv}\left(\mathbf{W}^{(m)}\right)\mathbf{S}^{(m)}\right)} \\
&\leq \min_{\theta\in\mathcal{I}} \frac{\mathrm{tr}\left(\mathbf{H}_\theta^\dagger \mathbf{W}^{(m)} \mathbf{H}_\theta \mathbf{S}^{(m)}\right)}{\sigma_v^2 \,\mathrm{tr}\left(\mathbf{W}^{(m)}\right)\mathrm{tr}\left(\mathbf{S}^{(m)}\right)} \\
&= \min_{\theta\in\mathcal{I}} \frac{\mathrm{tr}\left(\mathbf{H}_\theta \mathbf{S}^{(m)} \mathbf{H}_\theta^\dagger \mathbf{W}^{(m)}\right)}{\sigma_v^2 \,\mathrm{tr}\left(\mathbf{W}^{(m)}\right)} \qquad (37) \\
&\leq \min_{\theta\in\mathcal{I}} \frac{\mathrm{tr}\left(\mathbf{H}_\theta \mathbf{S}^{(m)} \mathbf{H}_\theta^\dagger\right)\mathrm{tr}\left(\mathbf{W}^{(m)}\right)}{\sigma_v^2 \,\mathrm{tr}\left(\mathbf{W}^{(m)}\right)} \qquad (38) \\
&\leq \min_{\theta\in\mathcal{I}} \frac{\mathrm{tr}\left(\mathbf{S}^{(m)}\right)\mathrm{tr}\left(\mathbf{H}_\theta^\dagger \mathbf{H}_\theta\right)}{\sigma_v^2} \qquad (39) \\
&= \frac{N}{\sigma_v^2} \min_{\theta\in\mathcal{I}} \left\|\mathbf{h}_\theta\right\|^2 .
\end{aligned}$$

In the first inequality, we used (14) to state:

$$\bar{\mathbf{\Sigma}}_{cv}\left(\mathbf{W}^{(m)}\right) \succeq \sigma_v^2 \,\mathrm{tr}\left(\mathbf{W}^{(m)}\right)\mathbf{I},$$

which leads to (37) because $\mathrm{tr}\left(\mathbf{S}^{(m)}\right) = 1$. Additionally, we employed the fact that for $\mathbf{A}, \mathbf{B} \succeq \mathbf{0}$:

$$0 \leq \mathrm{tr}(\mathbf{AB}) \leq \mathrm{tr}(\mathbf{A})\,\mathrm{tr}(\mathbf{B}),$$

to derive (38) and (39). Finally, $\mathrm{tr}\left(\mathbf{H}_\theta^\dagger \mathbf{H}_\theta\right)$ is simply the sum of the squared norms of the columns of $\mathbf{H}_\theta$. Given the structure of $\mathbf{H}_\theta$, this can be expressed as $\mathrm{tr}\left(\mathbf{H}_\theta^\dagger \mathbf{H}_\theta\right) = N\left\|\mathbf{h}_\theta\right\|_2^2$. Therefore, the upper bound on the sequence $\mathrm{SINR}^{(m)}$ is:

$$\mathrm{SINR}^{(m)} \leq \frac{N}{\sigma_v^2} \min_{\theta\in\mathcal{I}} \left\|\mathbf{h}_\theta\right\|_2^2 . \qquad (40)$$

Given the finite energy assumption for the TIR, inequality (40) combined with the monotonic increasing property of $\left\{\mathrm{SINR}^{(m)}\right\}$ ensures the convergence of the objective function sequence. ■

References

[1] C.-Y. Chen and P. P. Vaidyanathan, "MIMO radar waveform optimization with prior information of the extended target and clutter," *IEEE Transactions on Signal Processing*, vol. 57, no. 9, pp. 3533–3544, 2009.

[2] P. Wang, D. Han, Y. Cao, W. Ni, and D. Niyato, "Multi-objective optimization-based waveform design for multi-user and multi-target MIMO-ISAC systems," *IEEE Transactions on Wireless Communications*, vol. 23, no. 10, pp. 15 339–15 352, 2024.
[3] J. Hu *et al.*, "Constant modulus waveform design for MIMO radar via manifold optimization," *Signal Process.*, vol. 190, p. 108322, 2022.
[4] X. Cheng, J. Hu, Y. Wang, X. Cheng, K. Zhong, H. Li, J. Liu, and R. Wang, "Codesign of constant modulus waveform and receive filters for polarimetric radar," *IEEE Geoscience and Remote Sensing Letters*, vol. 21, pp. 1–5, 2024.
[5] Y. Yao, P. Miao, H. Liu, and Z.-M. Chen, "Robust transceiver design for extended target detection in a signal-dependent interference scenario," *IEEE Access*, vol. 8, pp. 122 292–122 303, 2020.
[6] S. M. Karbasi, A. Aubry, A. De Maio, and M. H. Bastani, "Robust transmit code and receive filter design for extended targets in clutter," *IEEE Transactions on Signal Processing*, vol. 63, no. 8, pp. 1965–1976, 2015.
[7] D. S. Ganesh and R. R. Kumar, "A MIMO moving target detection radar with optimal transmit and receive weightage," *Signal Processing*, vol. 208, p. 108978, 2023.
[8] S. G. Dontamsetti and R. V. R. Kumar, "A distributed MIMO radar with joint optimal transmit and receive signal combining," *IEEE Transactions on Aerospace and Electronic Systems*, vol. 57, no. 1, pp. 623–635, 2021.
[9] L. Wu, P. Babu, and D. P. Palomar, "Transmit waveform/receive filter design for MIMO radar with multiple waveform constraints," *IEEE Transactions on Signal Processing*, vol. 66, no. 6, pp. 1526–1540, 2018.
[10] M. M. Naghsh, M. Soltanalian, P. Stoica, M. Modarres-Hashemi, A. De Maio, and A. Aubry, "A Doppler robust design of transmit sequence and receive filter in the presence of signal-dependent interference," *IEEE Transactions on Signal Processing*, vol. 62, no. 4, pp. 772–785, 2014.
[11] A. De Maio and A. Farina, "Waveform diversity: past, present, and future," universita di Napoli Federico II (Italy) Dipartimento di Ingegneria, Tech. Rep., 2009.
[12] F. Yin, C. Debes, and A. M. Zoubir, "Parametric waveform design using discrete prolate spheroidal sequences for enhanced detection of extended targets," *IEEE Transactions on Signal Processing*, vol. 60, no. 9, pp. 4525–4536, 2012.
[13] A. Nehorai, F. Gini, M. S. Greco, A. P. Suppappola, and M. Rangaswamy, "Introduction to the issue on adaptive waveform design for agile sensing and communication," *IEEE Journal of Selected Topics in Signal Processing*, vol. 1, no. 1, pp. 2–5, 2007.
[14] W. Yuxi, H. Guoce, and L. Wei, "Waveform design for radar and extended target in the environment of electronic warfare," *Journal of Systems Engineering and Electronics*, vol. 29, no. 1, pp. 48–57, 2018.
[15] M. Bell, "Information theory and radar waveform design," *IEEE Transactions on Information Theory*, vol. 39, no. 5, pp. 1578–1597, 1993.
[16] R. A. Romero and N. A. Goodman, "Waveform design in signal-dependent interference and application to target recognition with multiple transmissions," *IET radar, sonar & navigation*, vol. 3, no. 4, pp. 328–340, 2009.
[17] G. Capraro, A. Farina, H. Griffiths, and M. Wicks, "Knowledge-based radar signal and data processing: a tutorial review," *IEEE Signal Processing Magazine*, vol. 23, no. 1, pp. 18–29, 2006.
[18] Z. Xu, Z. Xie, C. Fan, and X. Huang, "Probabilistically robust radar waveform design for extended target detection," *IEEE Transactions on Signal Processing*, vol. 70, pp. 4212–4224, 2022.
[19] S. Pillai, D. Youla, H. Oh, and J. Guerci, "Optimum transmit-receiver design in the presence of signal-dependent interference and channel noise," in *Conference Record of the Thirty-Third Asilomar Conference on Signals, Systems, and Computers (Cat. No.CH37020)*, vol. 2, 1999, pp. 870–875 vol.2.
[20] Z. Xu *et al.*, "Probabilistically robust design of radar waveform-filter for extended target detection in the presence of clutter," *IEEE Transactions on Signal Processing*, vol. 71, pp. 3267–3280, 2023.
[21] S. P. Sira, Y. Li, A. Papandreou-Suppappola, D. Morrell, D. Cochran, and M. Rangaswamy, "Waveform-agile sensing for tracking," *IEEE Signal Processing Magazine*, vol. 26, no. 1, pp. 53–64, 2009.

[22] N. A. Goodman *et al.*, "Adaptive waveform design and sequential hypothesis testing for target recognition with active sensors," *IEEE Journal of Selected Topics in Signal Processing*, vol. 1, no. 1, pp. 105–113, 2007.

[23] S. M. Sowelam and A. H. Tewfik, "Optimal waveform selection for target classification," in *1996 8^{th} European Signal Processing Conference (EUSIPCO 1996)*, 1996, pp. 1–4.

[24] X. Cheng, L. Wu, D. Ciuonzo, and W. Wang, "Joint design of horizontal and vertical polarization waveforms for polarimetric radar via SINR maximization," *IEEE Transactions on Aerospace and Electronic Systems*, vol. 59, no. 3, pp. 3313–3328, 2023.

[25] L. Wu, X. Cheng, H. Huang, D. Ciuonzo, B. Shankar, and B. Ottersten, "Constant-modulus waveform design with polarization-adaptive power allocation in polarimetric radar," *IEEE Transactions on Signal Processing*, vol. 71, pp. 2146–2161, 2023.

[26] M. R. Bell, "Information theory and radar waveform design," *IEEE Transactions on Information Theory*, vol. 39, no. 5, pp. 1578–1597, Sep. 1993.

[27] Y. Wei, H. Meng, Y. Liu, and X. Wang, "Radar waveform design for extended target recognition under detection constraints," *Mathematical Problems in Engineering*, vol. 2012, 02 2012.

[28] Y. Yang and R. S. Blum, "MIMO radar waveform design based on mutual information and minimum mean-square error estimation," *IEEE Transactions on Aerospace and Electronic Systems*, vol. 43, no. 1, pp. 330–343, Jan. 2007.

[29] B. Tang, J. Liu, H. Wang, and Y. Hu, "Constrained radar waveform design for range profiling," *IEEE Transactions on Signal Processing*, vol. 69, pp. 1924–1937, 2021.

[30] S. Haykin, "Cognitive radar: A way of the future," *IEEE Signal Processing Magazine*, vol. 23, no. 1, pp. 30–40, 2006.

[31] F. Dai *et al.*, "Adaptive waveform design for range-spread target tracking," *Electronics Letters*, vol. 46, no. 11, pp. 793–794, May 2010.

[32] M. Soltanalian, B. Tang, J. Li, and P. Stoica, "Joint design of the receive filter and transmit sequence for active sensing," *IEEE Signal Processing Letters*, vol. 20, no. 5, pp. 423–426, 2013.

[33] H. Hayvaci, A. Maio, and D. Erricolo, "Improved detection probability of a radar target in the presence of multipath with prior knowledge of the environment," *IET Radar, Sonar and Navigation*, vol. 7, pp. 36–46, 01 2013.

[34] A. Aubry, A. Maio, M. Piezzo, A. Farina, and M. Wicks, "Cognitive design of the receive filter and transmitted phase code in reverberating environment," *Radar, Sonar & Navigation, IET*, vol. 6, pp. 822–833, 12 2012.

[35] A. Aubry, A. DeMaio, A. Farina, and M. Wicks, "Knowledge-aided (potentially cognitive) transmit signal and receive filter design in signal-dependent clutter," *IEEE Transactions on Aerospace and Electronic Systems*, vol. 49, no. 1, pp. 93–117, 2013.

[36] B. Tang and J. Tang, "Robust waveform design of wideband cognitive radar for extended target detection," in *IEEE International Conference on Acoustics, Speech, and Signal Processing*, 2016, pp. 3096–3100.

[37] B. Jiu, H. Liu, D. Feng, and Z. Liu, "Minimax robust transmission waveform and receiving filter design for extended target detection with imprecise prior knowledge," *Signal Processing*, vol. 92, no. 1, pp. 210–218, 2012.

[38] Y. Yang and R. S. Blum, "Minimax robust MIMO radar waveform design," *IEEE Journal of Selected Topics in Signal Processing*, vol. 1, no. 1, pp. 147–155, Jun. 2007.

[39] M. Nouiehed, M. Sanjabi, T. Huang, J. Lee, and M. Razaviyayn, "Solving a class of non-convex min-max games using iterative first order methods," in *Neural Information Processing Systems*, 2019.

[40] M. Razaviyayn, T. Huang, S. Lu, M. Nouiehed, M. Sanjabi, and M. Hong, "Nonconvex min-max optimization: Applications, challenges, and recent theoretical advances," *IEEE Signal Processing Magazine*, vol. 37, no. 5, pp. 55–66, 2020.

[41] C. Jin, P. Netrapalli, and M. Jordan, "What is local optimality in nonconvex-nonconcave minimax optimization?" in *Proceedings of the 37th International Conference on Machine Learning*, ser. Proceedings of Machine Learning Research, H. D. III and A. Singh, Eds., vol. 119. PMLR, 13–18 Jul

2020, pp. 4880–4889.
[42] L. Chen, X. Qin, Y. Chen, and N. Zhao, "Joint waveform and clustering design for coordinated multi-point dfrc systems," *IEEE Transactions on Communications*, vol. 71, no. 3, pp. 1323–1335, 2023.
[43] M. I. Skolnik, *Radar Handbook*. New York, NY, USA: McGraw-Hill, 1990.
[44] L. K. Patton and B. D. Rigling, "Autocorrelation and modulus constraints in radar waveform optimization," in *Proceedings of the IEEE International Waveform Diversity and Design Conference*, 2009, pp. 150–154.
[45] M. M. Naghsh, M. Soltanalian, P. Stoica, M. Modarres-Hashemi, A. De Maio, and A. Aubry, "A doppler robust design of transmit sequence and receive filter in the presence of signal-dependent interference," *IEEE Trans. Signal Process.*, vol. 62, no. 4, pp. 772–785, 2014.
[46] Z.-q. Luo, W.-k. Ma, A. M.-c. So, Y. Ye, and S. Zhang, "Semidefinite relaxation of quadratic optimization problems," *IEEE Signal Processing Magazine*, vol. 27, no. 3, pp. 20–34, 2010.
[47] S. Quegan, "Spotlight synthetic aperture radar: Signal processing algorithms." *Journal of Atmospheric and Solar-Terrestrial Physics*, vol. 59, pp. 597–598, 1997.
[48] J. B. Keller, "Geometrical theory of diffraction," *Josa*, vol. 52, no. 2, pp. 116–130, 1962.
[49] C. Bachman, "Some recent developments in rcs measurement techniques," *Proceedings of the IEEE*, vol. 53, no. 8, pp. 962–972, 1965.
[50] Y. Yao, A. Farina, and Y. Li, "Robust transmit-receive optimization design for extended target detection," in *2020 IEEE 7th International Workshop on Metrology for AeroSpace (MetroAeroSpace)*, 2020, pp. 22–27.
[51] J. Bai, M. Zhang, and H. Zhang, "An inexact ADMM for separable nonconvex and nonsmooth optimization," *Computational Optimization and Applications*, pp. 1–35, 2025.
[52] K. Guo, D. Han, D. Z. Wang, and T. Wu, "Convergence of ADMM for multi-block nonconvex separable optimization models," *Frontiers of Mathematics in China*, vol. 12, pp. 1139–1162, 2017.
[53] J. Bai, J. Li, F. Xu, and H. Zhang, "Generalized symmetric ADMM for separable convex optimization," *Computational optimization and applications*, vol. 70, no. 1, pp. 129–170, 2018.
[54] C. Zhang, Y. Song, X. Cai, and D. Han, "An extended proximal ADMM algorithm for three-block nonconvex optimization problems," *Journal of Computational and Applied Mathematics*, vol. 398, p. 113681, 2021.
[55] Z. Liu, "Nonconvex ADMM for rank-constrained matrix sensing problem," *arXiv preprint arXiv:2310.00660*, vol. v2, 2023.
[56] Y. Wang, W. Yin, and J. Zeng, "Global convergence of ADMM in nonconvex nonsmooth optimization," *Journal of Scientific Computing*, vol. 78, pp. 29–63, 2019.
[57] H. Zhang, J. Gao, J. Qian, J. Yang, C. Xu, and B. Zhang, "Linear regression problem relaxations solved by nonconvex ADMM with convergence analysis," *IEEE Transactions on Circuits and Systems for Video Technology*, vol. 34, no. 2, pp. 828–838, 2024.
[58] H. Zhang, J. Yang, F. Shang, C. Gong, and Z. Zhang, "LRR for subspace segmentation via tractable schatten- p norm minimization and factorization," *IEEE Transactions on Cybernetics*, vol. 49, no. 5, pp. 1722–1734, 2019.
[59] H. Zhang, J. Yang, J. Qian, G. Gao, X. Lan, Z. Zha, and B. Wen, "Efficient image classification via structured low-rank matrix factorization regression," *IEEE Transactions on Information Forensics and Security*, vol. 19, pp. 1496–1509, 2024.
[60] Z. Xu, C. Fan, and X. Huang, "MIMO radar waveform design for multipath exploitation," *IEEE Transactions on Signal Processing*, vol. 69, pp. 5359–5371, 2021.
[61] M. Grant and S. Boyd, "CVX: MATLAB software for disciplined convex programming, version 2.1," Mar. 2014.
[62] N. Boumal and P.-A. Absil, "Low-rank matrix completion via preconditioned optimization on the Grassmann manifold," *Linear Algebra and its Applications*, vol. 475, pp. 200–239, 2015. [Online]. Available: https://www.sciencedirect.com/science/article/pii/S0024379515001342
[63] N. Boumal and P.-a. Absil, "RTRMC: A Riemannian trust-region method for low-rank matrix completion," *Advances in neural information processing systems*, vol. 24, 2011.

[64] G. Meyer, S. Bonnabel, and R. Sepulchre, "Linear regression under fixed-rank constraints: A Riemannian approach." 01 2011, pp. 545–552.

[65] J. Li, G. Liao, Y. Huang, Z. Zhang, and A. Nehorai, "Riemannian geometric optimization methods for joint design of transmit sequence and receive filter on MIMO radar," *IEEE Transactions on Signal Processing*, vol. 68, pp. 5602–5616, 2020.

[66] S. Gorshkov, S. Leshchenko, V. Orlenko, and S. Sedyshev, *Radar Target Backscattering Simulation: Software and User's Manual*, ser. Radar Library. Artech House, 2002.

[67] J. D. Shirman, *Computer Simulation of Aerial Target Radar Scattering, Recognition, Detection, Tracking.* Norwood, MA, USA: Artech House, 2002.